Available online at www.sciencedirect.com

ScienceDirect

Ceramics International 40 (2014) 715–722

CERAMICS INTERNATIONAL

www.elsevier.com/locate/ceramint

Densification behavior of Spark Plasma Sintered La_2O_3–YSZ ceramic composites

K.D. Robles Arellano[a], L. Bichler[a,*], K. Akkiraju[b], R. Fong[c], K. Mondal[a,d]

[a]School of Engineering, University of British Columbia—Okanagan, 3333 University Way, Kelowna, Canada V1V 1V7
[b]Department of Metallurgical and Materials Engineering, Indian Institute of Technology, Chennai 600036, India
[c]Atomic Energy of Canada Limited, Chalk River Laboratories, Chalk River, Ontario, Canada K0J 1J0
[d]Department of Materials Science and Engineering, Indian Institute of Technology, Kanpur 208016, India

Received 28 March 2013; received in revised form 6 June 2013; accepted 17 June 2013
Available online 26 June 2013

Abstract

The present paper describes the fabrication and densification behavior of 8 mol% Yttria-stabilized Zirconia (YSZ)-based composites with the addition of 11.6, 21.6 and 30.5 wt% La_2O_3 fabricated by the Spark Plasma Sintering (SPS) process. Addition of La_2O_3 to YSZ had a significant grain refining effect on the YSZ ceramic. In all of the studied composites, the desirable cubic structure of the YSZ matrix was retained and 94–96% densification was achieved. The matrix of the sintered composites evolved a solid solution due to interdiffusion of La, Zr and Y, as well as formation of pyrochlore lanthanate $La_{1.6}Y_{0.4}Zr_2O_7$ phase formed as the reaction product between YSZ and La_2O_3 during sintering.

Keywords: A. Sintering; B. Composite; B. Grain size; D. ZrO_2

1. Introduction

Zirconia (ZrO_2) is an attractive ceramic for engineering applications due to its very good high temperature stability, chemical inertness, low thermal conductivity and high fracture toughness [1–5]. At room temperature, ZrO_2 has a monoclinic structure, which undergoes a tetragonal phase transformation at 1170 °C followed by a cubic phase transformation at 2370 °C [6]. The densities of the monoclinic, tetragonal and cubic phases are 5.65 g/cm^3, 6.10 g/cm^3 and 6.27 g/cm^3 [7], respectively. Hence, the cubic to tetragonal and subsequently tetragonal to monoclinic phase transformations upon cooling from high temperature are often associated with volume expansion leading to large compressive residual stresses. This contributes to cracking of the as-sintered zirconia ceramic [6]. Suitable doping of ZrO_2 with divalent, trivalent or tetravalent ions, such as Ca^{2+}, Mg^{2+}, Al^{3+}, Y^{3+}, Ce^{4+}, enables stabilization of the cubic phase [8–13] and prevents undesirable cracking of the consolidated product. Due to the relative ease of fabrication, yttria-stabilized zirconia (YSZ) ceramics are now gaining technological importance.

Literatures [7,13–18] suggest that the addition of lanthanum dioxide (La_2O_3) to YSZ (up to 56 wt%) improves the thermal insulating properties of the composite, as well as promotes a strong grain refinement of the microstructure leading to enhanced mechanical properties [14]. Most available literatures [13–15,19] on the fabrication of La_2O_3–YSZ composites are limited to conventional sintering (CS) or preparation of coatings [7,16–18,20,21] using air spray pyrolysis and transfer arc plasma techniques. Some studies [7,15] have reported undesirable volume changes due to phase transformations upon cooling of the La_2O_3–YSZ composite. Challenges related to cracking, low density, as well as reaction of the composites with moisture in ambient air have been observed. Also, full stabilization of the La_2O_3–YSZ composites at low temperatures is highly challenging due to the large ionic radius of trivalent La^{3+} (103 pm) in comparison to that of Zr^{4+} (72 pm) [8]. Discrepancies in the literature about the microstructure evolution in the ceramic further hinder prediction of conclusive effects of lanthana addition to zirconia [7,13].

Recent studies indicate that zirconia-based composites prepared via Spark Plasma Sintering (SPS) can reach theoretical

*Corresponding author. Tel.: +1 250 807 8816; fax: +1 250 807 9850.
E-mail address: lukas.bichler@ubc.ca (L. Bichler).

0272-8842/$ - see front matter © 2013 Elsevier Ltd and Techna Group S.r.l. All rights reserved.
http://dx.doi.org/10.1016/j.ceramint.2013.06.060

densities >99% and ultra-fine grain size can be retained after SPS due to much lower sintering temperatures than typically used in CS [14,15,19,22–24]. Further, SPS offers rapid heating and densification, which leads to shorter sintering times in the range of 3–10 min [25–29], as well as the ability to sinter dissimilar materials [25,27,29] and possibly retain nano-structures [23,25]. However, there is a paucity of literature on SPS of lanthana-containing yttria-stabilized zirconia composites.

It the present work, La_2O_3–YSZ composites with the addition of 11.6, 21.6 and 30.5 wt% La_2O_3 were prepared by SPS process and their densification behavior was studied in detail. Microstructure and phase evolution during sintering were examined and related to the La_2O_3 doping level.

2. Experimental procedure

Precursor powders of 8 mol% (~13 wt%) yttria-stabilized zirconia (particle size 0.5 μm) and lanthanum dioxide (particle size 50–80 nm) with purity of 99.9% were obtained from Inframat Advanced Materials (CT, USA). The chemical composition of the precursor powders is provided in Table 1. Slurry blends of YSZ powder with the addition of 11.6, 21.6 and 30.5 wt% La_2O_3, respectively, were prepared in a beaker filled with alcohol. The slurries were dried for 24 h at room temperature in a desiccator. After drying, the powders were ground for 20 min using a pestle.

Blended powders were sintered using a Thermal Technologies Spark Plasma Sintering machine (Model 10-3) at Quad City Manufacturing Labs, USA. The powders were placed in a 19 mm diameter graphite die with a graphite foil lining. Sintering of all composite powders was carried out at a temperature of 1500 °C with uniaxial pressure of 50 MPa. The pressure was applied at the beginning of the heating cycle. Powders were heated to the sintering temperature at a rate of 100 K/min. After holding the sample for 10 min at the sintering temperature, the ram pressure was released and the composites were allowed to cool in the furnace. Upon ejection from the sintering die, the densities of the sintered composites were measured by the Archimedes' principle.

A Tescan MIRA3 XMU scanning electron microscope with Oxford X-max EDS detector were used for microstructural observation and chemical analysis. To reveal the grain width, subgrains and various phases within the composites, the samples were polished and thermally etched. Manual polishing of the samples was done using SiC and emery papers (grits 3/0 and 4/0) and a diamond paste (9 μm, 6 μm and 1 μm). Thermal etching (1 h) was carried out in air at 1450 °C. The grain size was subsequently measured via image analysis software (Buehler OmniMet) using the linear intercept method. X-ray diffraction (XRD) of the powders and as-sintered composites was carried out with the X'Pert Pro (PANalytical) X-Ray diffractometer with Bragg–Brentano set-up, equipped with X'Celeratrim in a 2θ range of 20–90° using 0.02° step size and 20 s time per step. Cu-K_α radiation with $\lambda = 1.541$ Å was used. Precision lattice parameter of the cubic phase was calculated using the Nelson-Riley technique [30].

3. Results and discussion

Fig. 1 shows the XRD patterns of the YSZ and La_2O_3 precursor powders, SPSed monolithic YSZ and SPSed La_2O_3–YSZ composites. The patterns in Fig. 1 confirmed that the original YSZ precursor powder had a cubic structure. Upon sintering of the monolithic YSZ and La_2O_3–YSZ powders, the matrix structure remained cubic. Interestingly, the addition of La_2O_3 did not destabilize the matrix and the SPS technique was successful in fabricating cubic La_2O_3–YSZ composites. However, there was a considerable shift towards a lower 2θ angle for the peaks of cubic YSZ, suggesting an increase in the lattice parameter of the cubic YSZ when La_2O_3 was added (Table 2). The peak shift in cubic YSZ also indicates that a solid solution formed between La_2O_3 and YSZ with accompanying lattice size expansion, since La^{3+} has a larger ionic radius than Zr^{4+}. Although the peaks corresponding to the monolithic La_2O_3 precursor powder could not be detected in the La_2O_3–YSZ composites, new peaks were detected in all of the sintered La_2O_3–YSZ composites. Based on detailed XRD

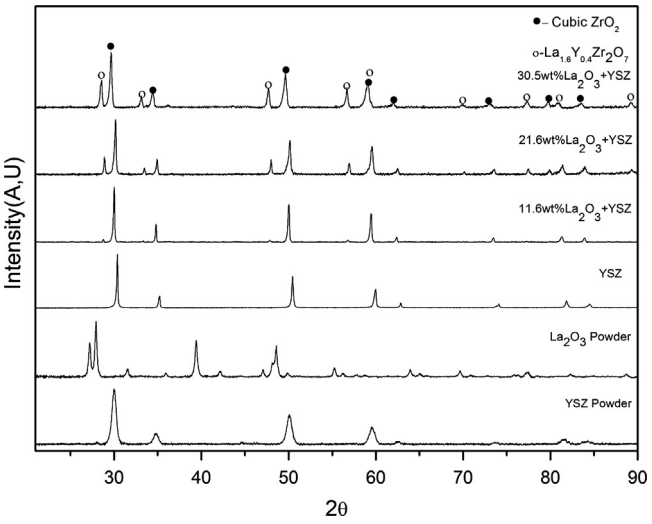

Fig. 1. XRD patterns of the SPS-processed composites.

Table 1
Chemical composition of precursor powders.

Precursor powder	Concentration (wt%)						Particle Size
	Zr	O	Y	La	Cl	Hf	(nm)
YSZ	60.4	28.7	8.8	–	0.7	1.3	500
La_2O_3	–	24.1	–	75.9	–	–	~80

analysis, the new peaks were identified as pyrochlore phase $La_{1.6}Y_{0.4}Zr_2O_7$, which likely formed through a reaction between YSZ and La_2O_3. Evolution of the pyrochlore $La_{1.6}Y_{0.4}Zr_2O_7$ phase was previously reported for 33 mol% (~56 wt%) La_2O_3+ZrO_2 composite processed at 1550 °C [31]. Fig. 2 shows the effect of La_2O_3 addition level on the relative density of the sintered composites. Relative density of ~92–96% was achieved in the composites manufactured via SPS at all La_2O_3 addition levels. However, it appeared that La_2O_3 addition to YSZ could possibly hinder the densification, since the relative density of the monolithic YSZ was 98%.

Table 2
Lattice parameters of the sintered YSZ and its composites.

Composite	Precision lattice parameter (Å)
Sintered YSZ	5.1358
11.6 wt% La_2O_3+YSZ	5.1597
21.6 mol% La_2O_3+YSZ	5.1604
30.5 mol% La_2O_3+YSZ	5.1675

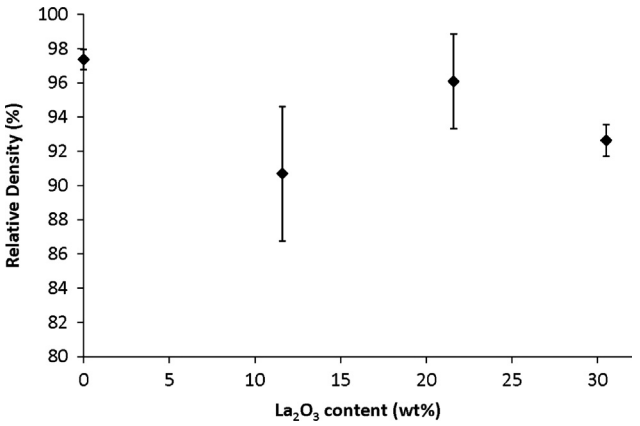

Fig. 2. Relative density of the as-sintered composites as a function of La_2O_3 content.

Fig. 3 shows representative SEM micrographs of the SPSed monolithic YSZ before and after annealing, respectively. The average grain size of the annealed composite was ~24 μm ± 1.26 μm. Since the as-received powder had the grain size of 0.5 μm, there was a considerable grain growth of the YSZ grains during sintering. As seen in Fig. 3, the grains in the monolithic YSZ had an equiaxed morphology. EDS chemical analysis of the YSZ matrix (Table 3) suggested that trace amounts of Cl and Hf were present. The Cl and Hf impurities were likely retained in the sintered YSZ from the raw precursor powders (Table 1). However, at local points, trace amounts of carbon were also detected. The origin of C could be due to possible contamination either from the grafoil sheets used during sintering or from the carbon tape used to mount the sample in the SEM machine.

Fig. 4 shows the general microstructure of the 11.6 wt% La_2O_3+YSZ composite. At this La_2O_3 doping level, the YSZ matrix (A in Fig. 4(b)) contained elliptical shaped zones (~17 μm in width and ~140 μm in length). These elliptical zones and surrounding areas exhibited significant Z-contrast (in back-scatter SEM imaging mode). The center part of the elliptical zone (region C in Fig. 4(b)) was the brightest and was surrounded by a less bright interface enclosure (region B). A detailed EDS analysis of these regions revealed that the elliptical zones were rich in La (Table 4), with the center being ~75 wt% La. The total area fraction of these elliptical zones in the composite was measured to be ~8%. Based on their geometry, it is likely that the La-rich center regions consisted of multiple powder agglomerates pressed together during sintering.

The 11.6 wt% La_2O_3+YSZ composite exhibited a bimodal microstructure (Fig. 4(c)), with large YSZ matrix grains (~9.87 μm ± 1.21 μm in width) and secondary small La-rich grains (~0.94 μm ± 0.23 μm in width). From Fig. 4(d) it could be observed that the small La-rich grains were generally located along the grain boundaries and at the grain triple points, which were energetically preferred zones for nucleation of second phases. As observed in Fig. 4(c) and (d), void formation along the grain boundaries was minimal, suggesting good bonding of adjacent grains in the sintered composite.

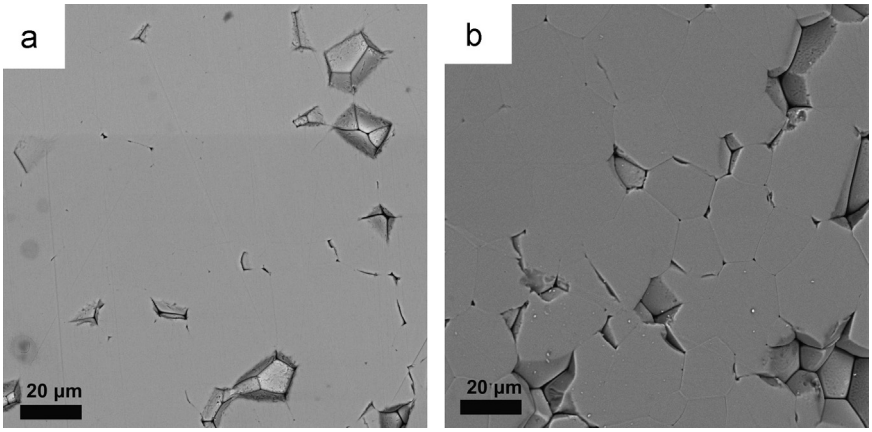

Fig. 3. SEM-BSE micrographs of the monolithic YSZ composites (a) as-sintered and (b) annealed.

Table 3
Chemical composition of the monolithic YSZ composite.

Location	Zr	Y	O	Cl	Hf
Matrix	62	8.5	21	< 0.1	1.4

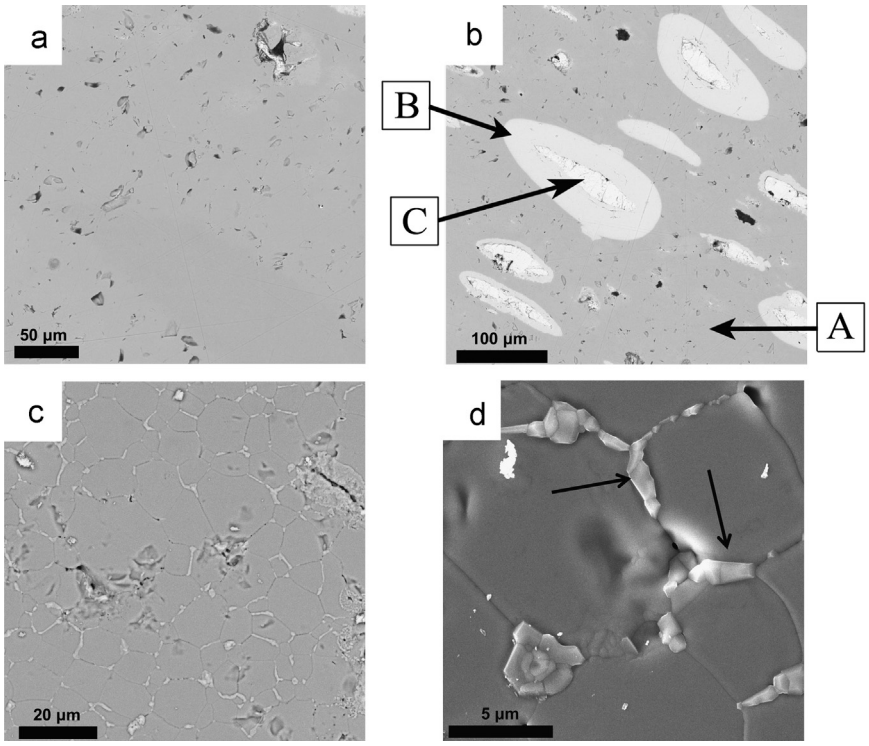

Fig. 4. SEM-BSE micrographs of the 11.6 wt% La_2O_3+YSZ composite (a) matrix, (b) elliptical La-rich zones, (c) bimodal microstructure and (d) small grains (shown by arrows).

Table 4
Chemical composition of the 11.6 wt% La_2O_3+YSZ composite.

Location	Region of interest	Zr	Y	La	O	Cl	Hf
A	Matrix	64	9.7	3.6	16	< 0.1	1.5
B	Elliptical zone interface region	30	3.8	51	11	0	0.7
C	Elliptical zone center region	0.1	0.1	75	5.4	15	< 0.1
–	Large YSZ grains	58	8.8	3.6	18	< 0.1	1.4
–	Small La-rich grains	48	6.4	16	18	< 0.1	1.1

Fig. 5(a)–(d) shows the SEM micrographs of the 21.6 wt% La_2O_3+YSZ composite. With the increase in the La_2O_3 content, the total area fraction of elliptical zones increased to ~29%. Fig. 5(c) and (d) shows the bimodal microstructure of the composite, which again consisted of large YSZ matrix grains (~6.73 μm ± 0.51 μm in width) and secondary small La-rich grains (~1.28 μm ± 0.16 μm in width). Thus, the large YSZ matrix grains in the 21.6 wt% La_2O_3+YSZ composite were smaller than the large YSZ matrix grains in the 11.6 wt% La_2O_3+YSZ composite. In contrast, the small La-rich grains grew in size, and remained located along the grain boundaries and at the triple points. In addition, as shown in Fig. 5(d), there were multiple occasions where the small La-rich grains began to form in the interior of the large YSZ matrix grains. The edges of the small grains were clearly delineated in comparison to the small grains in the 11.6 wt% La_2O_3+YSZ composite. Thus, increase in the La_2O_3 doping level resulted in the growth of the small La-rich grains, as well as their enhanced nucleation and growth throughout the matrix. In addition, it appeared that initial addition of La_2O_3 had hindered the YSZ grain growth (Fig. 2).

The chemical composition of the features in the 21.6 wt% La_2O_3+YSZ composite is summarized in Table 5. Since the processing parameters for all composites were the same, the higher content of La in the matrix regions likely originated from the higher La_2O_3 doping level. It was also observed in

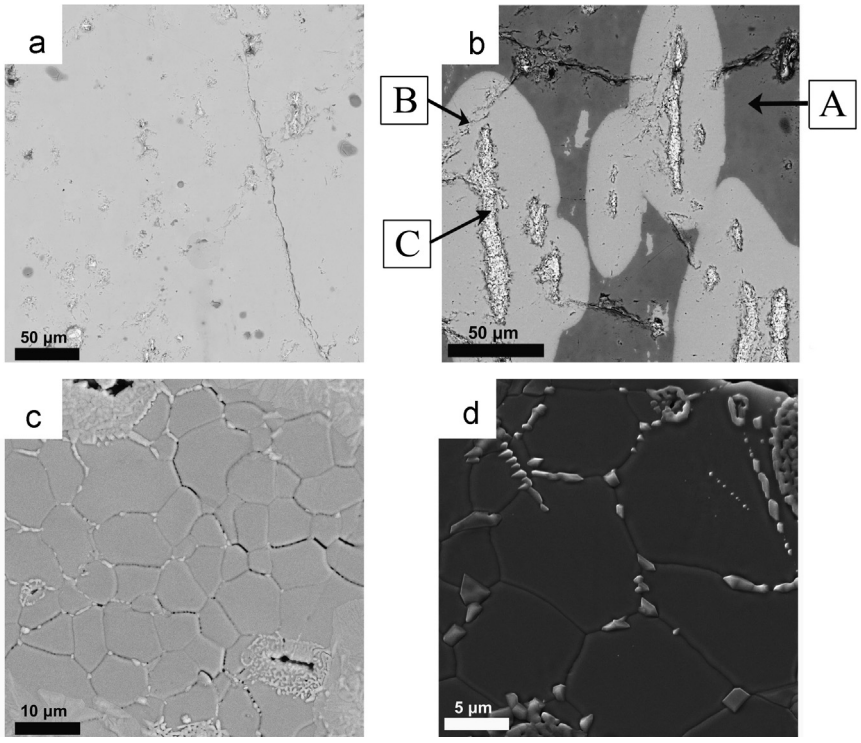

Fig. 5. SEM-BSE micrographs of the 21.6 wt% La_2O_3+YSZ composite (a) matrix, (b) elliptical La-rich zones, (c) bimodal microstructure and (d) small grains.

Fig. 5(b) that the center of the elliptical zones in this composite consisted of distinct particles, suggesting possibility of formation of agglomerates of La_2O_3 powder particles. A line scan as indicated in Fig. 6 showed a gradual variation in La, Zr and Y counts across a representative elliptical zone. The La content was maximum in the zone center and it decreased towards the matrix. In contrast, the contents of Zr and Y were minimum in the zone center and gradually increased across the interface towards the matrix. Thus, the presence of La in the gray zones and Zr and Y in the brighter zones suggested that there was interdiffusion of Zr, Y and La around the La_2O_3 agglomerates.

Fig. 7(a) shows the general microstructure of the as-sintered 30.5 wt% La_2O_3+YSZ composite. Fig. 7(b) and (c) shows the details of regions A (primary YSZ matrix) and region B (secondary La-rich matrix) seen in Fig. 7(a). Fig. 7(d) shows a detail of a grain boundary region with clearly visible small La-rich grains. Interestingly, in this composite, the elliptical zones had nearly disappeared with only minimal agglomeration of La_2O_3, as indicated in Fig. 7(a) by double arrow. The chemical composition of the composite constituents is provided in Table 6. The primary YSZ matrix (region A) had a higher Zr and Y contents, but a lower La content than the secondary La-rich matrix (region B). A representative line scan provided in Fig. 8 clearly supports this observation. Comparing Figs. 4 and 7, it was noted that as the La_2O_3 content in the composites increased, the interdiffusion of solute was more effective due to higher solute drag, which likely influenced the microstructure evolution and hindrance to grain growth of YSZ grains in the La_2O_3-containing composites.

The small La-rich grains forming along the grain boundaries and triple points of the large YSZ primary matrix were also observed in the 30.5 wt% La_2O_3+YSZ composite. However, as Fig. 7(d) suggests, these small La-rich grains now also formed in the primary YSZ matrix grain interior. The average grain size of the large grains in the primary YSZ matrix was ~12.6 μm ± 1.40 μm, further indicating that addition of La_2O_3 has caused hindrance to grain growth of YSZ. The La-rich grains in the secondary matrix were ~5.4 μm ± 0.60 μm. The small La-rich grains at the YSZ matrix grain boundaries and triple points were 1.3 μm ± 0.20 μm in size. Thus, the addition of La_2O_3 up to 21.6 wt% resulted in hindrance to grain growth of the primary YSZ matrix, with concomitant formation of small La-rich particles at the grain boundaries. However, once the La_2O_3 content reached 30.5 wt%, the YSZ grains experienced excessive interdiffusion with La, resulting in diminishing effect of hindrance to grain growth (Fig. 7) of the primary matrix and formation of a secondary La-rich matrix. Therefore, controlled addition of La_2O_3 could lead to grain refinement likely via interdiffusion of Zr and La. The interdiffusion of Zr was most effective in the case of the 30.5 wt%La_2O_3+YSZ composite (Tables 4–6).

Observing the peak intensity of the pyrochlore phase in the composites (Fig. 1) suggested that the relative amount of this constituent increased with increasing addition of La_2O_3 to YSZ. As a result, it is believed that the bright zones in the composite likely represented the pyrochlore phase forming as a result of the considerable interdiffusion of Zr and La followed by chemical reaction during sintering. In addition, there was a considerable solid solution formation, as noted by the shift of the cubic YSZ peaks and associated increase of the YSZ lattice parameter (Table 2).

Although addition of La_2O_3 to YSZ had hindered grain growth during sintering, composites prepared in this research via SPS

Table 5
Chemical composition of the 21.6 wt% La_2O_3+YSZ composite.

Location	Region of interest	Zr	Y	La	O	Cl	Hf
A	Matrix	64	9.2	6.3	14	< 0.1	1.6
B	Particle interface region	28	3.4	45	8.3	0.1	0.7
C	Particle center region	4.9	0.8	72	5.8	13	0.2
–	Large YSZ grains	48	7.5	3.2	22	–	0.9
–	Small La-rich grains	47	6.7	7.2	23	< 0.1	0.8

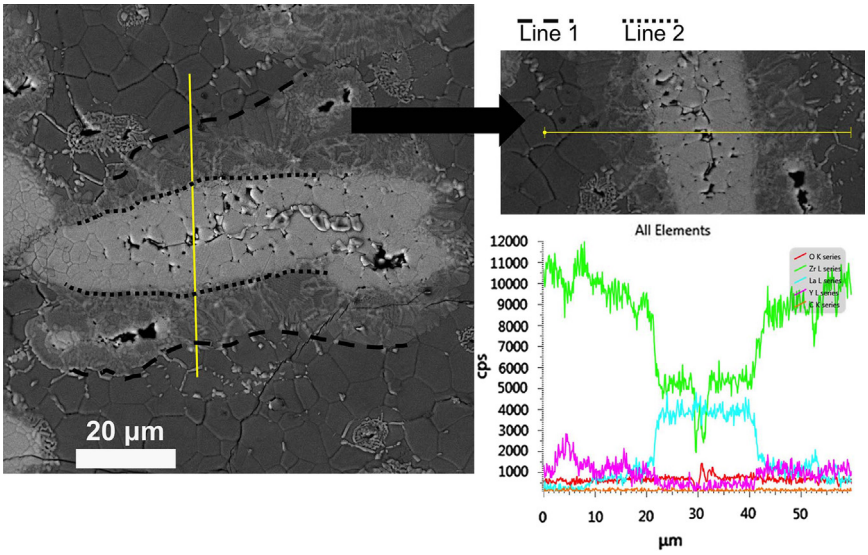

Fig. 6. Line-scan analysis of the elliptical La-rich zone in the 21.6 wt% La_2O_3+YSZ composite.

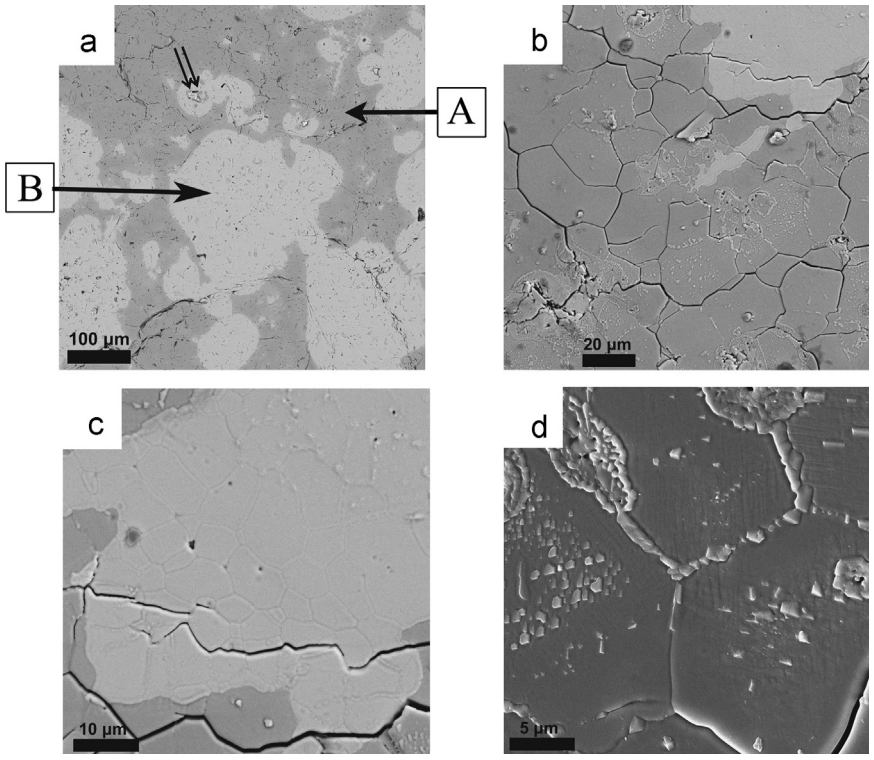

Fig. 7. SEM-BSE micrographs of the 30.5 wt% La_2O_3+YSZ composite (a) primary and secondary matrices, (b) large grains in primary matrix, (c) large grains in secondary matrix and (d) small grains.

Table 6
Chemical composition of the 30.5 wt% La_2O_3+YSZ composite.

Location	Region of interest	Zr	Y	La	O	Cl	Hf
A	Primary matrix	63	9.3	10	11	< 0.1	1.5
B	Secondary matrix	34	4.4	45	11	< 0.1	1
–	Large grains in primary YSZ matrix	49	7.6	5.6	25	< 0.1	0.9
–	Large grains in secondary La-rich matrix	29	3.8	34	22	< 0.1	0.7
–	Small La-rich grains	37	4.9	21	24	< 0.1	1

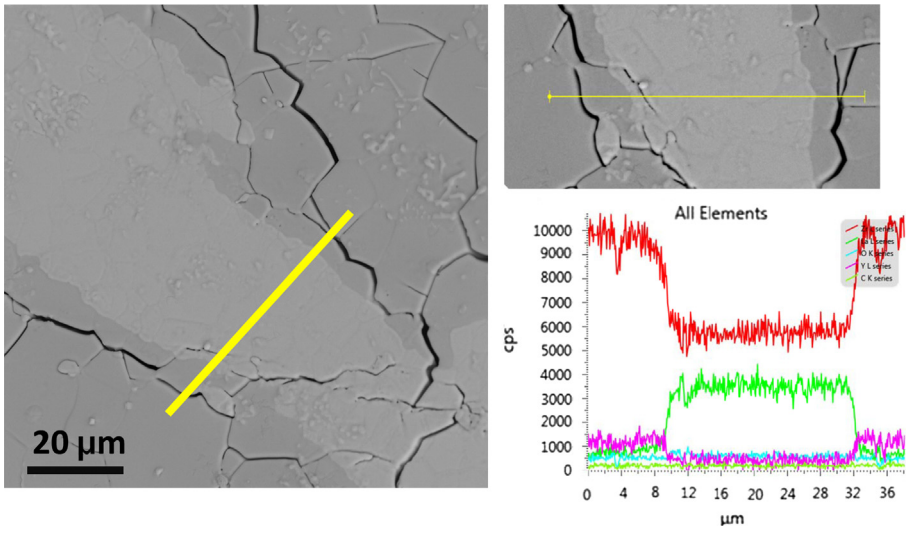

Fig. 8. Line-scan analysis of the secondary matrix in the 30.5 wt% La_2O_3+YSZ composite.

reached a relatively high level of densification (~92–96%) at process conditions of 1500 °C, 50 MPa and 10 min. In the case of pressureless sintering of YSZ and La_2O_3 green pellets, maximum densification (82%) was achieved at 1600 °C held for 2 h [32]. In the case of HIP processing of 8 mol% YSZ substituted $La_2Zr_2O_7$, a relative density of 99.7% was achieved at 1500 °C, 196 MPa for 2 h [21]. Thus, the present work clearly elucidates the ability of SPS to achieve optimal relative density of La_2O_3+YSZ composites at significantly lower time, pressure and temperature process conditions than those used in pressureless sintering or HIP.

Conclusions

Composites of 8 mol% yttria-stabilized zirconia doped with 11.6, 21.6, and 30.5 wt% La_2O_3 were successfully fabricated in the present work by Spark Plasma Sintering. A relative density level of 92–96% was achieved with the addition of up to 30.5 wt % La_2O_3. Further, in comparison to CS and HIP sintering techniques, the SPS approach allowed for the fabrication of relatively dense La_2O_3–YSZ composites at significantly lower temperature, pressure and shorter sintering times. Addition of La_2O_3 had a significant influence on the grain morphology and microstructure evolution of the composites. The grain size distribution in the composites was bimodal in nature. There was considerable hindrance to grain growth of YSZ grains due to the addition of La_2O_3 to the composites. The grain modification was associated with the interdiffusion of La and Zr. Up to the addition level of 21.6 wt% La_2O_3, significant interdiffusion of La and Zr likely resulted in a growth restriction effect of the primary matrix grains and concomitant grain refinement. At higher doping level, rapid interdiffusion of La and Zr enabled the formation of a secondary La-rich matrix.

Acknowledgments

The authors wish to acknowledge Mr. M. vanHanegem, Ms. A. Siebert-Timmer and Mr. D. Arkinstall from the University of British Columbia, Prof. B. S. Murty and Mr. S. Ipe Varghese from the Indian Institute of Technology Madras for their assistance with XRD analysis and SPS processing. The authors would also like to thank NSERC for providing the funding necessary to carry out this research.

References

[1] T. Xu, J. Vleugels, O. Van der Biest, P. Wang, Mechanical properties of Nd_2O_3/Y_2O_3-coated zirconia ceramics, Materials Science and Engineering A 374 (2004) 239–243.
[2] Z. Xu, L. He, X. Zhong, R. Mu, S. He, X. Cao, Thermal barrier coating of lanthanum–zirconium–cerium composite oxide made by electron beam-physical vapor deposition, Journal of Alloys and Compounds 478 (2009) 168–172.
[3] M. Kilo, C. Argirusis, G. Borchardt, S. Ghosh, A.H. Chokshi, Creep in scandia stabilized zirconia, Solid State Ionics 179 (2008) 804–806.

[4] J. Wolfenstine, Creep resistance comparison of two solid oxygen fuel cell electrolytes with the fluorite structure: cubic zirconia and doped-ceria, Journal of Power Sources 111 (2002) 173–175.
[5] X.Q. Cao, R. Vassen, D. Stoever, Ceramic materials for thermal barrier coatings, Journal of the European Ceramic Society 24 (2004) 1–10.
[6] O.A. Graeve, Ch 10: zirconia, in: J.F. Shackelford, R.H. Doremus (Eds.), Ceramic and Glass Materials: Structure, Properties and Processing, Springer, New York, 2008, pp. 169–197.
[7] S.A. Tsipas, Effect of dopants on the phase stability of zirconia-based plasma sprayed thermal barrier coatings, Journal of the European Ceramic Society 30 (2010) 61–72.
[8] J. Wolfenstine, Intrinsic creep resistance of two solid oxygen fuel cell electrolytes cubic zirconia vs. doped lanthanum gallate, Electrochemical and Solid-State Letters 2 (1999) 210–211.
[9] M.P. Harmer, H.M. Chan, J.M. Rickman, J. Cho, C.M. Wang, Grain boundary chemistry and creep resistance of oxide ceramics, Key Engineering Materials 161–163 (1999) 139–144.
[10] J.A. Allemann, B. Michel, H.-B. Märki, L.J. Gauckler, E.M. Moser, Grain growth of differently doped zirconia, Journal of the European Ceramic Society 15 (1995) 951–958.
[11] P.E. Evans, Creep in yttria- and scandia-stabilized zirconia, Journal of the American Ceramic Society 53 (1969) 365–369.
[12] R.G. St-Jaques, R. Angers, CaO-stabilized ZrO_2, Journal of the American Ceramic Society 55 (1972) 571–574.
[13] B. Bastide, Phase equilibrium and martensitic transformation in lanthana-doped zirconia, Journal of the American Ceramic Society 71 (1988) 449–453.
[14] P. Singh, S.R. Sainkar, M.V Kuber, V.G. Gunjikar, R.F. Shinde, S. K. Date, La-stabilized zirconia: synthesis and characterization, Materials Letters 9 (1990) 65–70.
[15] C. Wang, O. Fabrichnaya, M. Zinkevich, Y. Du, F. Aldinger, Experimental study and thermodynamic modelling of the ZrO_2–$LaO_{1.5}$ system, Calphad 32 (2008) 111–120.
[16] S.B. Weber, H.L. Lein, T. Grande, M.-A. Einarsrud, Deposition mechanisms of thick lanthanum zirconate coatings by spray pyrolysis, Journal of the American Ceramic Society 94 (2011) 4256–4262.
[17] S. Yugeswaran, A. Kobayashi, P.V. Ananthapadmanabhan, L. Lusvarghi, Influence of processing variables on the formation of $La_2Zr_2O_7$ in transferred arc plasma torch processing, Current Applied Physics 11 (2011) 1394–1400.
[18] C.S. Ramachandran, V. Balasubramanian, P.V. Ananthapadmanabhan, Synthesis, spheroidization and spray deposition of lanthanum zirconate using thermal plasma process, Surface and Coatings Technology 206 (2012) 3017–3035.
[19] C. Wang, Y. Wang, Y. Cheng, W. Huang, Z.S. Khan, X. Fan, Y. Wang, B. Zou, X. Cao, Preparation and thermophysical properties of nano-sized $Ln_2Zr_2O_7$ (Ln=La, Nd, Sm, and Gd) ceramics with pyrochlore structure, Journal of Materials Science 47 (2012) 4392–4399.
[20] C.S. Ramachandran, V. Balasubramanian, P.V. Ananthapadmanabhan, V. Viswabaskaran, Influence of the intermixed interfacial layers on the thermal cycling behaviour of atmospheric plasma sprayed lanthanum zirconate based coatings, Ceramics International 38 (2012) 4081–4096.
[21] A. Ota, Y. Matsumura, M. Yoshinaka, K. Hirota, O. Yamaguchi, Formation and sintering of 8mol% Y_2O_3-substututed $La_2Zr_2O_7$ by the hydrazine method, Journal of Materials Science Letters 17 (1998) 199–201.
[22] M. Omori, Sintering, consolidation, reaction and crystal growth by the Spark Plasma System (SPS), Materials Science and Engineering A 287 (2000) 183–188.
[23] Y. Bangchao, J. Jiawen, Z. Yican, Spark-plasma sintering the 8-mol% yttria-stabilized zirconia electrolyte, Journal of Materials Science 39 (2004) 6863–6865.
[24] P. Dahl, I. Kaus, Z. Zhao, M. Johnsson, M. Nygren, K. Wiik, T. Grande, M.A. Einarsrud, Densification and properties of zirconia prepared by three different sintering techniques, Ceramics International 33 (2007) 1603–1610.
[25] Y.J. Wu, J. Li, X.M. Chen, K. Kakegawa, Densification and microstructures of $PbTiO_3$ ceramics prepared by spark plasma sintering, Materials Science and Engineering A 257 (2010) 5157–5160.
[26] K.A. Khor, L.-G. Yu, S.H. Chan, X.J. Chen, Densification of plasma sprayed YSZ electrolytes by spark plasma sintering (SPS), Journal of the European Ceramic Society 23 (2003) 1855–1863.
[27] X. He, F. Ye, H. Zhang, L. Liu, Study of rare-earth oxide sintering additive systems for Spark Plasma Sintering AlN ceramics, Materials Science and Engineering A 527 (2010) 5268–5272.
[28] L. Ceja-Cárdenas, J. Lemus-Ruíz, D. Jaramillo-Vigueras, S.D. de la Torre, Spark plasma sintering of α-Si_3N_4 ceramics with Al_2O_3 and Y_2O_3 as additives and its morphology transformation, Journal of Alloys and Compounds 478 (501) (2010) 345–351.
[29] F. Ye, Z. Hou, H. Zhang, L. Liu, Y. Zhou, Spark plasma sintering of cBN/β-SiAlON composites, Materials Science and Engineering A 527 (2010) 4723–4726.
[30] J.B. Nelson, D.P. Riley, An experimental investigation of extrapolation methods in the derivation of accurate unit-cell dimensions of crystals, Proceedings of the Physical Society 57 (1945) 160–177.
[31] A.V. Rhada, S.V. Ushakov, A. Navrotsky, Thermochemistry of lanthanum zirconate pyrochlore, Journal of Materials Research 24 (2009) 3350–3357.
[32] J.A. Labrincha, J.R. Frade, F.M.B. Marques, $La_2Zr_2O_7$ formed at ceramic electrode/YSZ contacts, Journal of Materials Science 28 (1993) 3809–3815.